



Hierarchical Hollow Co/N-C@NiCo₂O₄ Microsphere as an Efficient Bi-functional Electrocatalyst for Rechargeable Zn–Air Battery

Yuke Song[†], Wenfu Xie[†], Shijin Li, Jian Guo* and Mingfei Shao*

State Key Laboratory of Chemical Resource Engineering, Beijing University of Chemical Technology, Beijing, China

OPEN ACCESS

Edited by:

Zhenhai Xia,
University of North Texas,
United States

Reviewed by:

Shichun Mu,
Wuhan University of
Technology, China
Bao Yu Xia,
Huazhong University of Science and
Technology, China

*Correspondence:

Jian Guo
guojian@mail.buct.edu.cn
Mingfei Shao
shaomf@mail.buct.edu.cn

[†]These authors have contributed
equally to this work

Specialty section:

This article was submitted to
Energy Materials,
a section of the journal
Frontiers in Materials

Received: 18 August 2019

Accepted: 01 October 2019

Published: 25 October 2019

Citation:

Song Y, Xie W, Li S, Guo J and
Shao M (2019) Hierarchical Hollow
Co/N-C@NiCo₂O₄ Microsphere as an
Efficient Bi-functional Electrocatalyst
for Rechargeable Zn–Air Battery.
Front. Mater. 6:261.
doi: 10.3389/fmats.2019.00261

Zn–air batteries (ZABs) have drawn extensive attention for portable and wearable electronic devices owing to their high theoretical specific energy density and low cost. However, due to the dense packing under high mass loading, the mass/charge diffusion is seriously hindered, making their practical performance with high power density, and energy density difficult to sustain. Herein, we reported an efficient bi-functional electrocatalyst of Ni-Co mixed metal oxides incorporated with cobalt/nitrogen-doped carbon with hierarchical hollow nanostructure (H-Co/N-C@NiCo₂O₄). Benefiting from the advantages of this structure and composition, the H-Co/N-C@NiCo₂O₄ exhibits superior electrocatalytic activity and long-time durability for both oxygen reduction reaction (ORR) and oxygen evolution reaction (OER). The potential gap between half-wave potential in ORR and overpotential at a current density of 10 mA cm⁻² in OER reaches 0.8 V, much smaller than that of most reported bi-functional electrocatalysts. Moreover, H-Co/N-C@NiCo₂O₄ is constructed as an air electrode for rechargeable ZAB, delivering a high power density and long cycling stability. The good linear relationship between the power density and various mass loading of H-Co/N-C@NiCo₂O₄ on the electrode demonstrates that the performance has been well-maintained even under high dense packing of catalysts, which offers a new pathway for the practical applications in ZAB.

Keywords: bi-functional electrocatalyst, ORR and OER, synergetic effect, hierarchical hollow nanostructure, zinc–air battery

INTRODUCTION

Zinc–air batteries (ZABs) have been investigated tremendously in past decades owing to their promising theoretical specific energy density of 1,086 Wh kg⁻¹ and low cost, which would meet the ever-increasing energy requirements for renewable energy conversion devices (Lee et al., 2011; Li and Dai, 2014; Chen et al., 2018; Meng et al., 2018; Wang H. F. et al., 2018; Wang T. et al., 2018). Despite these advantages, the sluggish kinetics of oxygen reduction reaction (ORR) and oxygen evolution reaction (OER) during discharging and charging at the air-cathode always result in limited energy and power density of the devices in practical applications (Prabu et al., 2014; Park et al., 2017; Jiang H. et al., 2018; Liu et al., 2019; Qiu et al., 2019). To solve the above problems, a large number of electrocatalysts have been developed for high performance of ORR or OER, such as noble metals (Wu et al., 2010; Audichon et al., 2016), transition metals/metal oxides (Fu et al., 2018; Li T. et al., 2018), and metal-free materials (Ferrero et al., 2016; Hang et al., 2018).

However, these catalytically active materials generally face issues regarding activities for ORR and OER simultaneously and stabilities (Guo Z. et al., 2018). Thus, exploring highly efficient, stable bi-functional oxygen electrocatalysts is still an urgent task for the ZABs.

Transition metal composites [e.g., oxides (Guan C. et al., 2017; Li Y. et al., 2018; Peng et al., 2018, sulfides (Zhou et al., 2013, 2017b; Ganesan et al., 2015; Zhang et al., 2016), and phosphides (Zhou et al., 2017a; Wu et al., 2018) have been highlighted as attractive candidates for OER electrocatalysts, but they fail to catalyze the ORR process. Recently, heteroatom-doped carbon materials expressed excellent electrocatalytic activity for ORR, where Co–N–C has been regarded as one of the best candidates for ORR and Zn–air batteries (Zhao et al., 2012; Shang et al., 2016; Amiinu et al., 2018; Guo Y. et al., 2018; Jiang R. et al., 2018; Wang T. et al., 2018; Wang Z. et al., 2018; Liang et al., 2019). Being inspired by this, assembling transition metal oxides with heteroatom-doped carbon materials is an effective approach to obtain bi-functional electrocatalysts for both OER and ORR (Guo Z. et al., 2018). However, in practice, the performance of electrocatalysts under high mass loading is difficult to maintain due to the agglomeration of particles that severely inhibits mass/charge diffusion process, which has so far been few considered (Xie et al., 2019). Therefore, it is desirable to construct advanced electrodes with more sophisticated functionalities, so as to boost mass transfer process and more exposed active sites under high catalyst loading.

Herein, we demonstrate a bi-functional electrocatalyst with well-ordered hierarchical hollow nanostructure, which shows high performances for both the ORR and OER even under high mass loading. The bi-functional hollow structured electrocatalyst consisting of cobalt/nitrogen-doped carbon embedded with Ni–Co mixed metal oxides (H–Co/N–C@NiCo₂O₄) is prepared *via* a facile self-template approach. Benefiting from the advantages of this structure and composition, the as-synthesized H–Co/N–C@NiCo₂O₄ exhibits impressive electrocatalytic activity and long-time durability for both ORR and OER. In addition, the advanced H–Co/N–C@NiCo₂O₄ is constructed as an air cathode for rechargeable ZAB, which delivers a high power density and long cycling stability. The good linear relationship between the power density and various mass loading of H–Co/N–C@NiCo₂O₄ on the electrode demonstrates that the performance has been well-maintained even under high dense packing of catalysts, which offers a new pathway for the practical applications in ZAB.

EXPERIMENTAL SECTION

Synthesis of PS@ZIF-67 Microsphere Template

Firstly, the polystyrene (PS) microsphere was synthesized using a method of dispersion polymerization (Lee et al., 2006). Then, the synthesized PS (0.25 g) and Co(NO₃)₂·6H₂O (2.25 g) were dispersed in methanol (150 ml). Then, 150 ml of methanol solution containing 6.225 g of 2-methylimidazole was quickly added into the former dispersion. After stirring at room

temperature for 1 h, the products were washed with methanol and dried overnight.

Synthesis of PS@ZIF-67@NiCo-LDH and PS@NiCo-LDH

Firstly, 0.2 g of PS@ZIF-67 was dispersed in 100 ml of ethanol. Then, 25 ml of ethanol solution containing 0.45 g of Ni(NO₃)₂·6H₂O was quickly poured into the former dispersion. After stirring at room temperature for 0.5 h, the products were washed with ethanol and dried overnight. The products were denoted as PS@ZIF-67@NiCo-LDH. Besides, PS@NiCo-LDH was also synthesized by using the above procedures but stirring for 4 h.

Synthesis of H-Co/N-C, H-Co/N-C@NiCo₂O₄, and H-NiCo₂O₄

The as-prepared PS@ZIF-67, PS@ZIF-67@NiCo-LDH, and PS@NiCo-LDH were pyrolyzed in N₂ at 600°C for 2 h. The products were denoted as H-Co/N-C, H-Co/N-C@NiCo₂O₄, and H-NiCo₂O₄, respectively.

Characterization

X-ray diffraction patterns were obtained on a Shimadzu XRD-6000 diffractometer with Cu K α radiation. Scanning electron microscope (SEM) was obtained on Zeiss Supra 55. Elemental mapping and EDS were recorded using energy-dispersive X-ray spectroscopy (EDS) attached to the SEM. High-resolution transmission electron microscope (HRTEM) was performed on JEOL JEM-2010. X-ray photoelectron spectra (XPS) were collected using a Thermo VG ESCALAB 250. Raman spectra were carried out by HORIBA Jobin Yvon Raman microspectrometer. N₂ adsorption/desorption isotherms were investigated using an Micromeritics ASAP 2020 instrument at 77 K.

Electrochemical Measurements

All electrochemical tests were carried out on an electrochemical workstation (CHI 760E, Shanghai Chenhua, China). A glassy carbon (GC) or carbon cloth with catalysts, Pt wire, and Ag/AgCl electrode were used as working electrode, counter electrode, and reference electrode, respectively. The catalyst inks were prepared as follows: 5.89 mg catalyst was ultrasonically dispersed in 770 μ l of deionized water, 200 μ l of ethanol, and 30 μ l of Nafion solution (5 wt%). For the ORR tests, the as-prepared catalyst ink was pipetted onto the rotating disk electrode (RDE, 0.196 cm²) and ring rotating disk electrode (RRDE, carbon disk with a surface area of 0.126 cm² surrounded by a Pt ring with a surface area of 0.224 cm²) with a loading of 0.3 mg cm⁻², and dried under room temperature. Cyclic voltammetry (CV) was tested in O₂- and N₂-saturated 0.1 M KOH at a scan rate of 100 mV s⁻¹. The following tests were obtained in O₂-saturated 0.1 M KOH. RDE tests were carried out at various rotation rates from 400 to 2,025 rpm with a scan rate of 5 mV s⁻¹. RRDE measurements were also conducted in O₂-saturated 0.1 M KOH at room temperature. The disk potential was scanned from -1 to 0.2 V at a scan rate of 5 mV s⁻¹ and the ring potential was constant at 0.5 V. The stability tests were measured by *i*-*t* amperometric response at 0.16 V vs.

RHE. RRDE tests, electrochemical impedance spectra (EIS), and $i-t$ amperometric response were all measured at a rotation rate of 1,600 rpm. The electrical double-layer capacitance (C_{dl}) of the catalysts was performed using CV at different scan rates from 20 to 120 mV s^{-1} in non-Faradaic region. For the OER tests, the catalyst ink was pipetted onto carbon cloth with a loading of 1 mg cm^{-2} , and dried under room temperature. Linear sweep voltammetry (LSV) was measured in 1 M KOH at a scan rate of 5 mV s^{-1} under stirring (90% iR -compensation).

The potential vs. reversible hydrogen electrode (RHE) was calculated via the Nernst equation:

$$E_{RHE} = E_{Ag/AgCl} + 0.059 \text{ pH} + 0.197$$

The overpotential (η) was calculated using the following formula:

$$\eta (\text{V}) = E_{RHE} - 1.23 \text{ V}$$

The electron transfer number (n) was calculated according the Koutecky–Levich equation:

$$\frac{1}{j} = \frac{1}{j_L} + \frac{1}{j_K} = \frac{1}{B\omega^{1/2}} + \frac{1}{j_K}$$

$$B = 0.62nFC_0D_0^{2/3}\nu^{-1/6}$$

where j , j_L , and j_K are the measured current density, diffusion-limiting current density, and kinetic current density, respectively; ω is the rate of electrode rotation speed; F is the Faraday constant ($96,485 \text{ C mol}^{-1}$); C_0 is the bulk concentration of O_2 ($1.26 \times 10^{-6} \text{ mol cm}^{-3}$); D_0 is the diffusion coefficient of O_2 in 0.1 M KOH ($1.9 \times 10^{-5} \text{ cm}^2 \text{ s}^{-1}$); ν is the kinematic viscosity of electrolyte ($0.01 \text{ cm}^2 \text{ s}^{-1}$).

For the RRDE measurements, the percentage of hydrogen peroxide yield HO_2^- (%) and the electron transfer number (n)

were calculated using the following formula:

$$\text{HO}_2^- (\%) = 200 \frac{I_r/N}{I_d + I_r/N}$$

$$n = 4 \frac{I_d}{I_d + I_r/N}$$

where I_d and I_r are the disk and ring currents, respectively; N is the ring collection efficiency determined to be 0.37.

The difference in current density ($\Delta j = j_a - j_c$) at 0.46 V vs. RHE was plotted against scan rate and fitted to a linear regression for the estimation of double layer capacitances (C_{dl}).

$$C_{dl} = \frac{\text{slope of regression line}}{2}$$

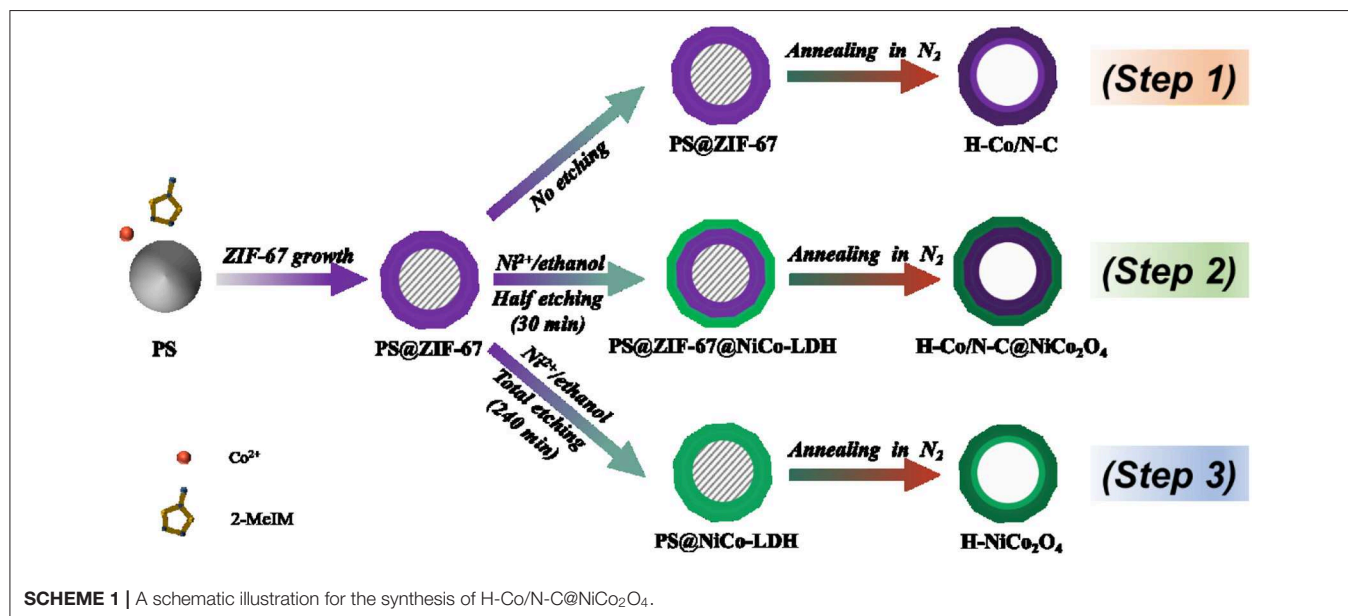
The Tafel slope was calculated by the following formula:

$$\eta = a + b \log |j|$$

where η is the overpotential; b is the Tafel slope; j is the current density.

Zn–Air Battery Tests

All Zn–air battery tests were carried out on an electrochemical workstation (CHI 660E, Shanghai Chenhua, China). A carbon cloth loaded with the catalyst inks (1 mg cm^{-2}) served as the air cathode, and a polished Zn foil served as the anode. For the rechargeable Zn–air batteries, 6 M KOH and 0.2 M $\text{Zn}(\text{CH}_3\text{COO})_2$ were chosen as the electrolyte. The polarization curves were measured at a scan rate of 5 mV s^{-1} . The galvanostatic charge and discharge cycling curves were measured at a current density of 5 mA cm^{-2} (discharge 100 s and charge 100 s). Specifically, discharging polarization curves at a current density of 10 mA cm^{-2} were measured in 6 M KOH.



The power density, specific capacity, and energy density were calculated by the following formula:

$$\text{Power density (mW cm}^{-2}\text{)} = \text{current density} \times \text{voltage}$$

$$\text{Specific capacity (mAh g}^{-1}\text{)} = \frac{\text{current} \times \text{service hours}}{\text{weight of consumed Zn}}$$

$$\text{Energy density (Wh kg}^{-1}\text{)} = \frac{\text{current} \times \text{service hours} \times \text{average discharge voltage}}{\text{weight of consumed Zn}}$$

RESULTS AND DISCUSSION

Material Characterizations

The synthesis process of hollow Co/N-C@NiCo₂O₄ microspheres (H-Co/N-C@NiCo₂O₄) is illustrated in **Scheme 1** (Step 2, see the Experimental Section for details). First, PS microspheres with an average size of 2.7 μm were synthesized *via* a dispersion polymerization process (**Figure 1a**). Second, zeolitic imidazolate framework (ZIF-67) nanoparticles were compactly assembled on the surface of PS to obtain PS@ZIF-67 microspheres (**Figures 1b, 2A**). The growth mechanism of ZIF-67 on the surface of PS microsphere is supposed to be the nucleation growth mechanism (Guan B. Y. et al., 2017). Typically, Co ions first coordinate with the carboxylate on the surface of PS microsphere. Then, 2-methylimidazole

connects with the Co ions and leads to the *in situ* nucleation process and the growth of ZIF-67 nanoparticles. Third, the obtained PS@ZIF-67 microspheres were *in situ* converted into PS@ZIF-67@NiCo-LDH microspheres by reacting with Ni(NO₃)₂ in ethanol solution for 30 min (**Figure 1c**). After that, the ZIF-67 nanoparticles with a dodecahedral shape partly dissolved and lots of nanosheets were aligned on the surface of microspheres, which derived a unique architecture of honeycomb with yolk-shelled structure. Last, a thermal treatment was performed to obtain hollow and hierarchical Co/N-C@NiCo₂O₄ microspheres (**Figure 1d**). After thermal treatment, the structure of microspheres is maintained while the average size of microspheres is decreased from 3.1 to 2.8 μm due to the contraction of ZIF-67. TEM image reveals that hollow cavities are formed inside H-Co/N-C@NiCo₂O₄ microspheres as a result of volatilization of PS (**Figure 1e**), which would facilitate the electrolyte penetration. High-resolution TEM image shows that lots of nanoparticles with an interlayer spacing of 4.7 and 2.9 Å dispersed on the surface of microsphere, corresponding to the (111) and (220) plane of NiCo₂O₄ (Zhang and Lou, 2013), which are derived from NiCo-LDH (**Figure 1f**). Other nanoparticles embedded in graphite-like layers with an interlayer spacing of 2.1 Å correspond to the (111) plane of Co metal (Aijaz et al., 2016). Moreover, the EDS elemental mapping of H-Co/N-C@NiCo₂O₄ displays a well-uniformed distribution of C, N, O, Co, and Ni, confirming the successful introduction of Ni during the etching process

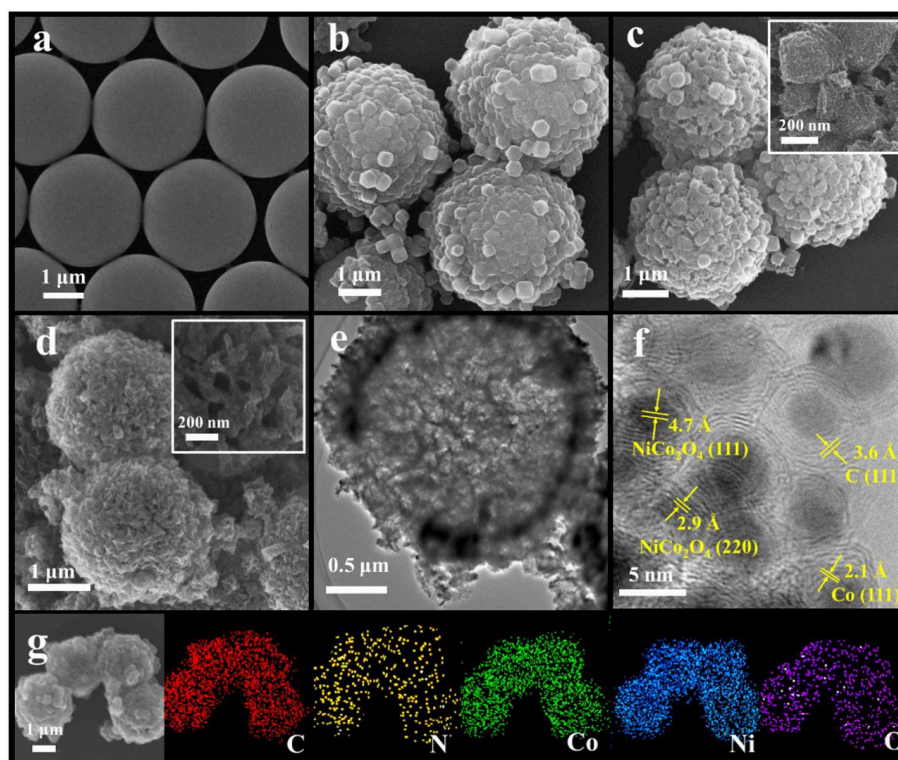
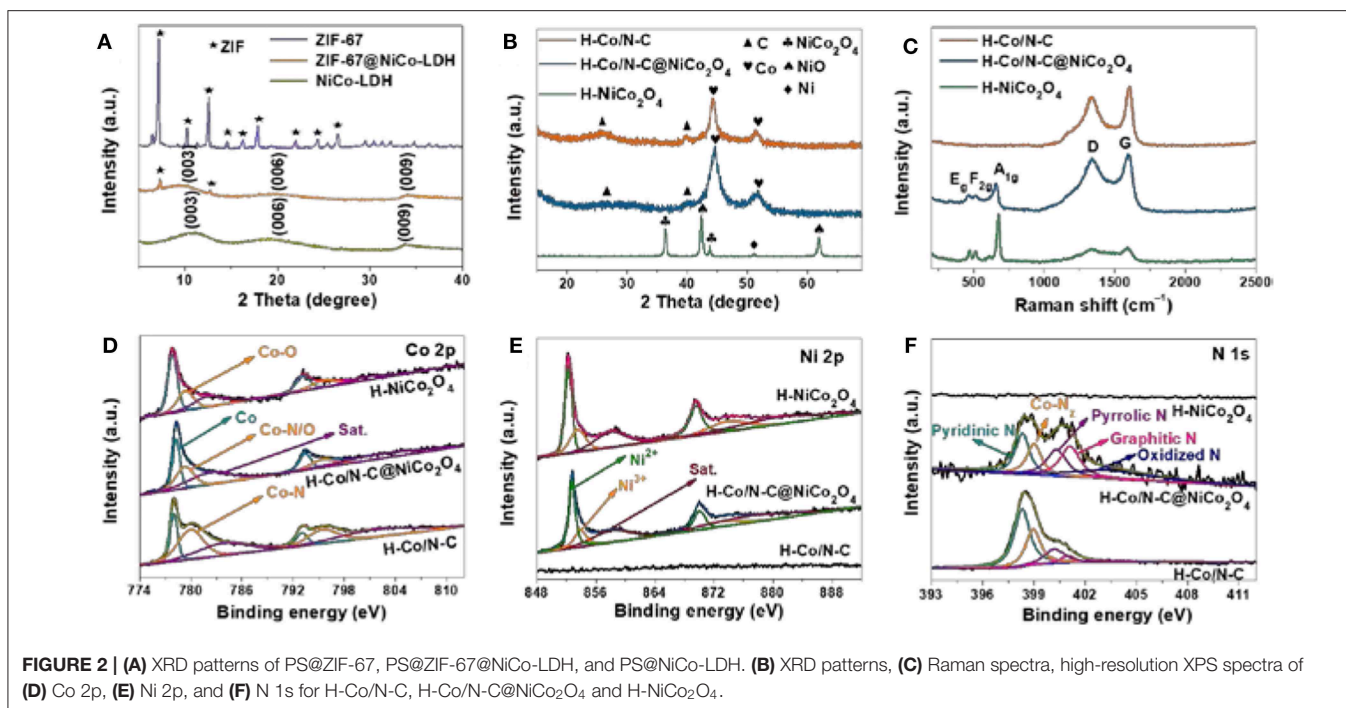


FIGURE 1 | SEM images of (a) PS microspheres, (b) PS@ZIF-67 microspheres, (c) PS@ZIF-67@NiCo-LDH microspheres, and (d) H-Co/N-C@NiCo₂O₄. (e) TEM and (f) HRTEM image of H-Co/N-C@NiCo₂O₄. (g) SEM and EDS elemental mapping images of H-Co/N-C@NiCo₂O₄.

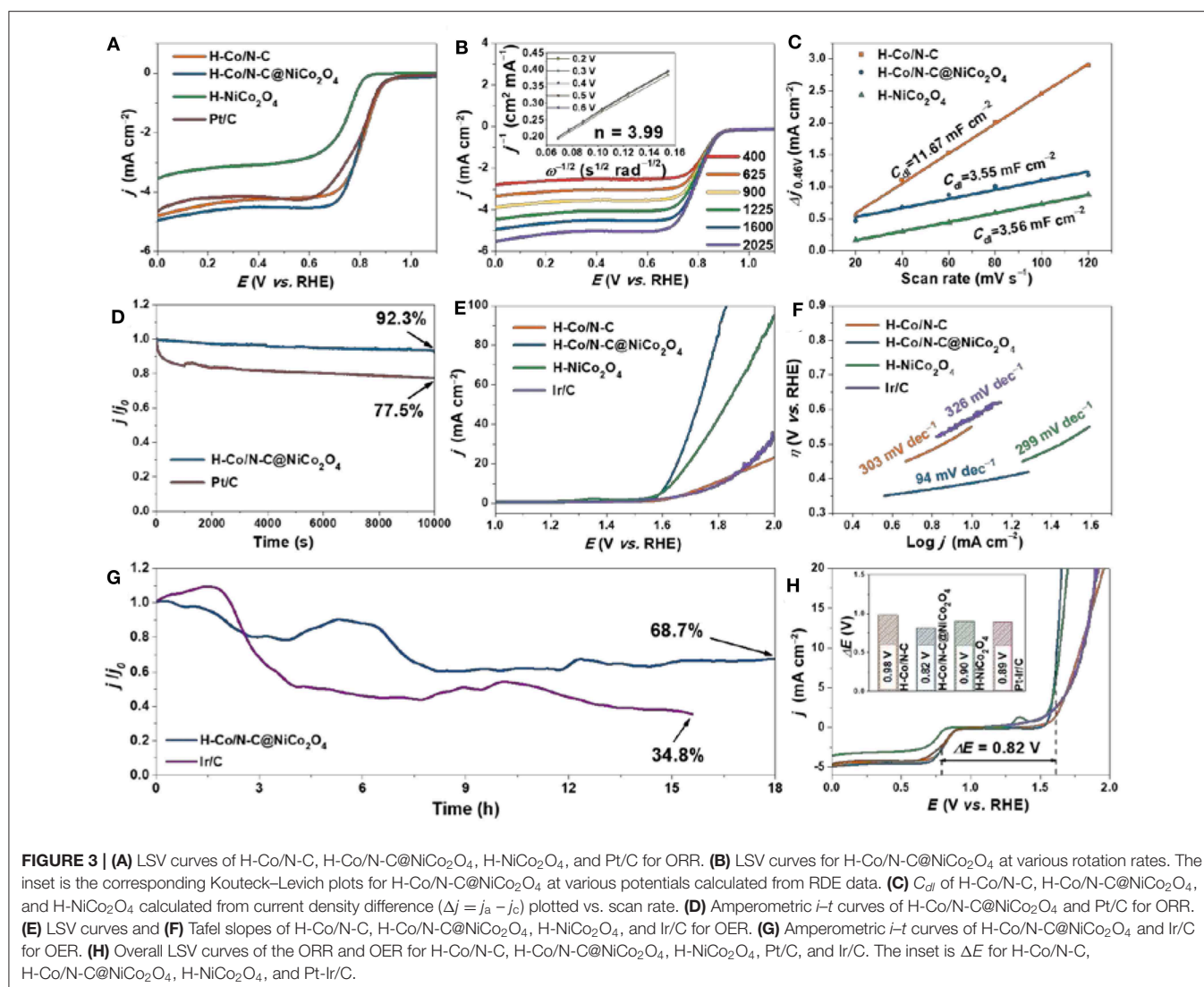


(Figure 1g and Figure S5). During the etching process, ZIF-67 could be completely etched away when the etching time is prolonged to 4 h and the product noted is as PS@NiCo-LDH [Scheme 1 (Step 3), Figures S1a, S2]. After thermal treatment, PS@NiCo-LDH is *in situ* transformed into hollow NiCo₂O₄ microspheres (denoted as H-NiCo₂O₄) (Figures S1b,c). In addition, hollow Co, N-doped carbon microspheres (denoted as H-Co/N-C) without NiCo₂O₄ obtained by direct pyrolysis of PS@ZIF-67 was also synthesized as reference [Scheme 1 (Step 1); Figures S3, S4].

XRD analysis of ZIF-67@NiCo-LDH indicates that ZIF-67 is successfully transformed into NiCo-LDH, from which the peaks of ZIF-67 are transformed into three peaks at $\sim 11^\circ$, 20° , and 34° , attributed to the (003), (006), and (009) planes of LDH (Li et al., 2015; Kaneti et al., 2017) (Figure 2A). After thermal treatment, the diffraction patterns of H-Co/N-C@NiCo₂O₄ and H-Co/N-C show that two well-defined diffraction peaks that emerged at 44.3° and 51.7° correspond to the (111) and (200) planes of face-centered Co (JCPDS15-0806), and the peaks at 26.1° and 44.6° are indexed to the (002) and (111) planes of graphitic carbon (Li J. et al., 2018). The diffraction pattern of H-NiCo₂O₄ implies the presence of NiCo₂O₄ (PDF#73-1702), NiO (PDF#89-7390), and Ni (PDF#70-0989). It should be mentioned that the diffraction peak of NiCo₂O₄ is not observed in H-Co/N-C@NiCo₂O₄ due to the high peak intensity of Co (Figure 2B). The graphitic feature and defects of synthesized materials were investigated by Raman spectra (Figure 2C). The intensity ratio of the D band (1340 cm^{-1}) to the G band (1590 cm^{-1}) (I_D/I_G) for H-Co/N-C@NiCo₂O₄ (0.95) is higher than H-Co/N-C (0.83), indicating that H-Co/N-C@NiCo₂O₄ contains more defective carbon, which is beneficial to the improvement

of electrocatalytic activity (Zhang et al., 2011; Chen et al., 2017; Yang et al., 2017; Asset et al., 2018). Besides, there are three peaks at 463 cm^{-1} (E_g mode), 507 cm^{-1} (F_{2g} mode), and 663 cm^{-1} (A_{1g} mode) in H-Co/N-C@NiCo₂O₄ and H-NiCo₂O₄, corresponding to Co-O and Ni-O molecular vibration peaks of NiCo₂O₄ (Umeshbabu et al., 2015).

The X-ray photoelectron spectroscopy (XPS) spectra confirm the presence of C, N, O, Co, and Ni in H-Co/N-C@NiCo₂O₄ (Figure S6 and Table S1). The Co 2p spectrum demonstrates the presence of both zero valence state (777.8 and 793.1 eV) and oxidation state (779.3 and 795.6 eV) Co species, which can be assigned to the metallic Co and Co-N/O_x coordination, respectively (Ni et al., 2017) (Figure 2D). For the Ni 2p spectrum of H-Co/N-C@NiCo₂O₄ and H-NiCo₂O₄, the peaks located at $852.2/869.5$ and $853.7/873.9\text{ eV}$ correspond to Ni³⁺ and Ni²⁺, respectively (Cui et al., 2009) (Figure 2E). The N 1s peak of H-Co/N-C@NiCo₂O₄ is deconvoluted into five types of N species, namely, pyridinic (398.5 eV), Co-N_x (399.6 eV), pyrrolic (400.5 eV), graphitic (401.0 eV), and oxidized (403.7 eV) N species (Jia et al., 2017) (Figure 2F). There is no N 1s peak in H-NiCo₂O₄, indicating that ZIF-67 is completely removed by etching. The surface area and pore size distribution of H-Co/N-C, H-Co/N-C@NiCo₂O₄, and H-NiCo₂O₄ are investigated by N₂-adsorption/desorption isotherms (Figure S7). The type IV isotherms with H₃-type hysteresis loops are observed for all samples, indicating the existence of mesopores (Li et al., 2016; Zhan and Zeng, 2017). Although the specific surface area of H-Co/N-C@NiCo₂O₄ is the smallest, it exhibits the best electrocatalytic performance in subsequent electrochemical tests, indicating that the synergy between Co/N-C and



NiCo₂O₄ is beneficial to the improvement of electrochemical properties (Table S2).

Oxygen Electrocatalysis Performance

The electrocatalytic activity of H-Co/N-C@NiCo₂O₄ toward ORR is assessed with a conventional three-electrode cell. To better demonstrate the superior activity of H-Co/N-C@NiCo₂O₄, the reference samples of H-Co/N-C, H-NiCo₂O₄, and commercial Pt/C were also evaluated and compared comprehensively. The raised cathodic peak at ~0.75 V vs. RHE in an O₂-saturated electrolyte compared to that in an N₂-saturated electrolyte indicates effective ORR electrocatalytic activity of synthesized materials (Figure S8). LSV curves (Figure 3A) display more positive onset-potential (0.913 V vs. RHE), half-wave potential (0.796 V vs. RHE), and larger diffusion-limited current density (-4.96 mA cm^{-2}) of H-Co/N-C@NiCo₂O₄ than that of H-Co/N-C, H-NiCo₂O₄, and commercial Pt/C (Table S3). The rotating disk electrode (RDE) was carried out to calculate the reaction kinetic parameters *via* Koutecky–Levich (K–L)

equation (Figure 3B and Figure S9). The calculated electron transfer number of H-Co/N-C@NiCo₂O₄ is 3.99, implying a direct four-electron process for ORR. Rotating ring disk electrode (RRDE) is operated to further quantify the ORR pathway of H-Co/N-C@NiCo₂O₄ (Figure S10). The results indicate that the HO₂⁻ yield of H-Co/N-C@NiCo₂O₄ is the smallest among all synthesized materials. Besides, the average electron transfer number of H-Co/N-C@NiCo₂O₄ is 3.61, larger than that of H-Co/N-C (3.51) and H-NiCo₂O₄ (2.40), which conform to the result obtained from K–L plots.

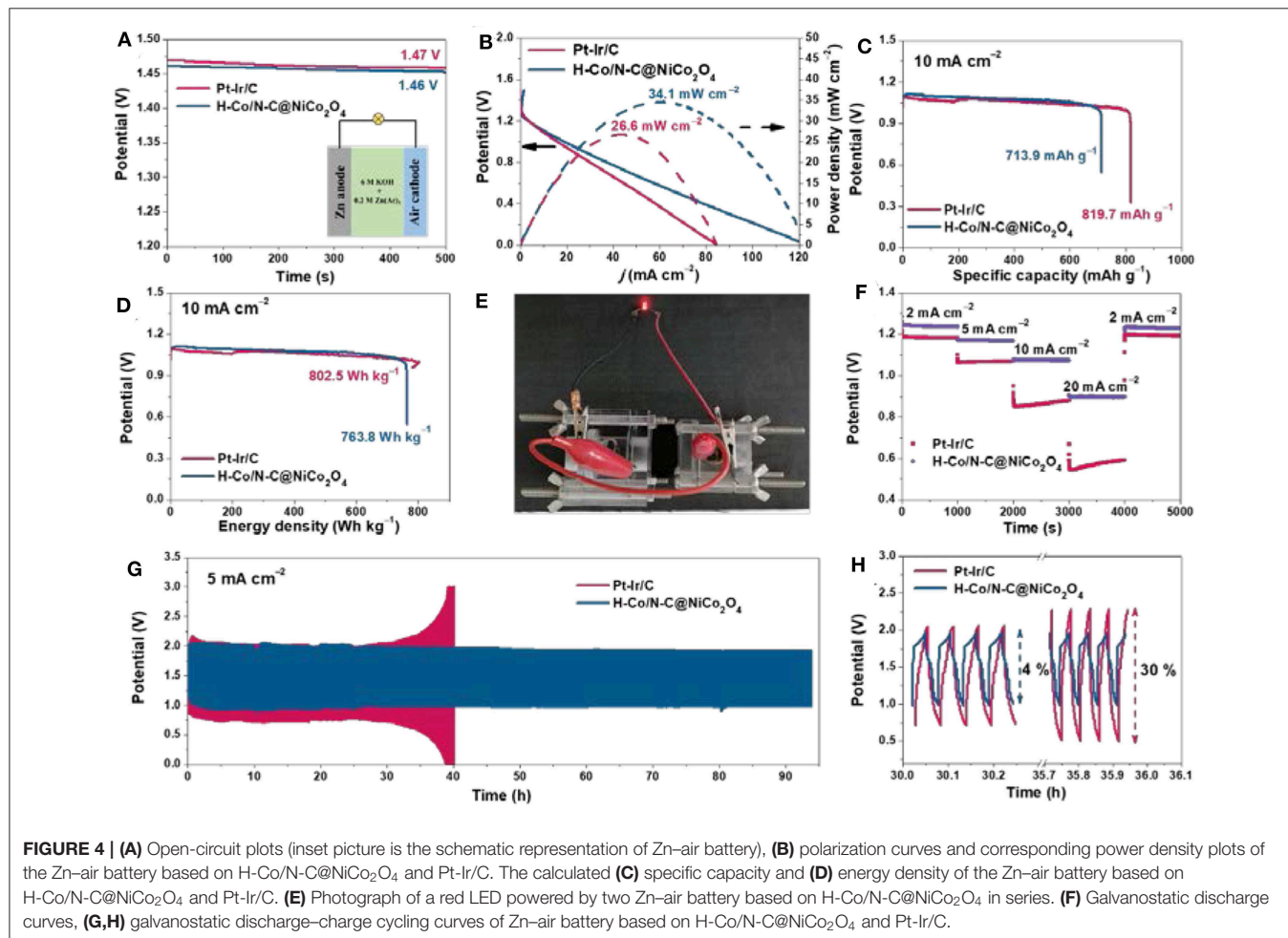
The electrochemical double-layer capacitance (C_{dl}) was deliberately measured to represent the relative electrochemical surface area (ECSA), which is linearly proportional to the number of active sites (Qiu et al., 2019) (Figure S11). The results in Figure 3C suggest that H-Co/N-C@NiCo₂O₄ exhibits the smallest C_{dl} value (3.55 mF cm^{-2}) compared with H-Co/N-C (11.67 mF cm^{-2}) and H-NiCo₂O₄ (3.56 mF cm^{-2}). This indicates that the largely promoted ORR activity is due to the synergetic effect of Co/N-doped carbon and NiCo₂O₄. Besides

the activity, stability is another important parameter for the practical applications of high-performance ORR electrocatalysts. The H-Co/N-C@NiCo₂O₄ shows an excellent durability with 92.3% retention after a continuous operation of 10,000 s, much more stable than that of commercial Pt/C catalysts (with only 77.5% retention) (**Figure 3D**), demonstrating a superb long-term stability of H-Co/N-C@NiCo₂O₄ toward ORR.

Furthermore, the OER performances are also investigated in KOH solution with 90% *iR*-compensation (**Figure 3E**). The H-Co/N-C@NiCo₂O₄ displays a relatively low onset potential with an overpotential of 386 mV to achieve the current density of 10 mA cm⁻², far superior to H-Co/N-C (552 mV), H-NiCo₂O₄ (405 mV), and commercial Ir/C (567 mV). Besides, H-Co/N-C@NiCo₂O₄ presents a Tafel slope of 94 mV dec⁻¹, much smaller than that of H-Co/N-C (303 mV dec⁻¹), H-NiCo₂O₄ (299 mV dec⁻¹), and commercial Ir/C (326 mV dec⁻¹), and reveals much faster reaction kinetics for OER (**Figure 3F**). Furthermore, the stability of H-Co/N-C@NiCo₂O₄ for OER was investigated (**Figure 3G**). Although performance has declined to some extent, which is the result of the dissolution of materials from carbon cloth due to the bubble formation, the H-Co/N-C@NiCo₂O₄ still retains 68.7% of the initial performance after continuous

operation of 18 h, better than that of Ir/C catalysts (with only 34.8% retention after 15 h), demonstrating the promising potential to replace noble metal catalysts for both ORR and OER. Additionally, the robust stability of H-Co/N-C@NiCo₂O₄ is verified by TEM, HRTEM, and XPS. As can be seen from **Figure S12**, the structure and composition retain their original state after all electrochemical tests, demonstrating the superior stability of H-Co/N-C@NiCo₂O₄. XPS measurement of H-Co/N-C@NiCo₂O₄ after all electrochemical tests exhibits some predictable changes (**Figure S13**). Namely, the valence state of Co and Ni has increased after all electrochemical tests, which is an unavoidable result after working at a high potential (Cao et al., 2018; Gu et al., 2018).

The overall oxygen electrode activity for both ORR and OER is evaluated by the difference between the overpotential measured at a current density of 10 mA cm⁻² for OER and half-wave potential for ORR ($\Delta E = E_{j10} - E_{1/2}$). Remarkably, the H-Co/N-C@NiCo₂O₄ displays a ΔE of 0.82 V, much lower than that of H-Co/N-C (0.98 V), H-NiCo₂O₄ (0.90 V), commercial Pt-Ir/C (0.89 V) (**Figure 3H**), and most reported bi-functional electrocatalysts (**Table S4**). The electrochemical performance of H-Co/N-C@NiCo₂O₄ and the control samples is



further investigated by electrochemical impedance spectroscopy measurements (Figure S14). From the Nyquist plots, the charge transfer resistance ($R_{ct} = \sim 9.8 \Omega$) of H-Co/N-C@NiCo₂O₄ and H-Co/N-C is nearly the same ($R_{ct} = \sim 9.8 \Omega$) at high frequency due to the excellent conductivity of N-doped carbon. However, the pure H-NiCo₂O₄ shows relative sluggish electron transfer ability ($R_{ct} = \sim 12.2 \Omega$) because of the limited conductivity. Moreover, the straight line at low frequency shows significantly increased slope for H-Co/N-C@NiCo₂O₄ than H-Co/N-C, indicating the faster mass diffusion behavior benefiting from this unique hierarchical structure. Although the mass diffusion ability is not as good as that of H-NiCo₂O₄, the better ORR performance of H-Co/N-C@NiCo₂O₄ indicates that the balance between mass diffusion and charge transfer is crucial for the performance of electrocatalysts.

The excellent ORR and OER performance of H-Co/N-C@NiCo₂O₄ benefits from the advantages of promoted surface reaction, enhanced charge transfer property, and improved mass diffusion process. As shown in Figure S15, the LSV plots of H-Co/N-C@NiCo₂O₄, H-Co/N-C, and H-NiCo₂O₄ for ORR were normalized by their ECSA. The current density of H-Co/N-C@NiCo₂O₄ ($-0.274 \text{ mA cm}^{-2} \text{ mF}^{-1}$) is much higher than that of H-Co/N-C ($-0.081 \text{ mA cm}^{-2} \text{ mF}^{-1}$) and H-NiCo₂O₄ ($-0.195 \text{ mA cm}^{-2} \text{ mF}^{-1}$), indicating high intrinsic activity for ORR owing to the synergistic effect between the compositions (Figure 3C and Figure S7). Second, the combination of H-Co/N-C and NiCo₂O₄ renders fast electron transfer between active sites and current collector, which can be verified by the lower resistance of $\sim 9.8 \Omega$ (Figure S14). Last but not least, the unique hierarchical hollow structure also ensures an efficient mass diffusion process, which accelerates the transport and adsorption of reactants to active sites and thus leads to a high reaction kinetics (Tafel slope of 94 mV dec^{-1}), better than that of H-Co/N-C

(303 mV dec^{-1}) and H-NiCo₂O₄ (299 mV dec^{-1}) (Figure 3F and Figure S14).

Encouraged by the superior electrochemical activity under basic medium, the ORR performance of H-Co/N-C@NiCo₂O₄ was also investigated in acidic medium (Figure S16). The H-Co/N-C@NiCo₂O₄ delivers acceptable ORR performance with a diffusion-limited current density of -3.06 mA cm^{-2} , better than that of H-NiCo₂O₄ (-2.47 mA cm^{-2}) and H-Co/N-C (-2.95 mA cm^{-2}). However, due to the instability behavior of NiCo₂O₄ under acidic conditions, this performance cannot be well-maintained for a long lifespan.

Zn–Air Battery Performance

Motivated by the superior electrocatalytic activity for both ORR and OER, the feasibility of H-Co/N-C@NiCo₂O₄ as the air cathode in Zn–air battery was further studied. The open-circuit voltage of Zn–air battery based on H-Co/N-C@NiCo₂O₄ is 1.46 V (Figure 4A), comparable to that of the Zn–air battery based on commercial Pt-Ir/C (1.47 V). The discharge polarization curve of the Zn–air battery based on H-Co/N-C@NiCo₂O₄ reveals a high peak power density of 34.1 mW cm^{-2} , which is superior to that of the Zn–air battery based on commercial Pt-Ir/C (26.6 mW cm^{-2}) (Figure 4B). Moreover, the Zn–air battery based on H-Co/N-C@NiCo₂O₄ delivers high specific capacity (713.9 mAh g^{-1}) and energy density (763.8 Wh kg^{-1}) at a current density of 10 mA cm^{-2} , respectively, close to that of Pt-Ir/C (819.7 mAh g^{-1} and 802.5 Wh kg^{-1}) (Figures 4C,D). A light-emitting diode could be effectively powered by two Zn–air batteries in series (Figure 4E). The discharge curves of Zn–air battery based on H-Co/N-C@NiCo₂O₄ and commercial Pt-Ir/C are conducted at various current densities from 2 to 20 mA cm^{-2} . Compared with the commercial Pt-Ir/C electrode, the H-Co/N-C@NiCo₂O₄ electrode shows higher discharge voltages and relatively stable discharge performance, indicating the better ORR activity, and reversible capacity (Figure 4F). Moreover, the H-Co/N-C@NiCo₂O₄ electrode shows excellent stability as there is only a small change in charge and discharge voltages (voltage gap increases by 4%) over 90 h in the long-term cycling tests, while the commercial Pt-Ir/C electrode shows a large change (voltage gap increases by 30%) after 36 h, which indicates the excellent stability and rechargeability of the Zn–air battery based on H-Co/N-C@NiCo₂O₄ (Figures 4G,H).

A most typical strategy to achieve high performance of a device system is to increase mass loading of electrocatalysts (Liu et al., 2018). However, the issues of physical limits to mass loading and plateau effect in performance are all inevitable (Xie et al., 2019). In this work, we further study the battery performance of H-Co/N-C@NiCo₂O₄ under high mass loading. Obviously, the peak power density of H-Co/N-C@NiCo₂O₄ gradually increases from 27.2 to 49.7 mW cm^{-2} with the increasing mass loading from 0.5 to 4 mg cm^{-2} (Figure 5A and Table S5), which demonstrates that most active sites could participate into the reaction in spite of the electrocatalyst layers becoming thicker (Figure 5B). This high mass-loading-independent performance of H-Co/N-C@NiCo₂O₄ is largely ascribed to the following hierarchical structure features and compositional merits. First, the synergistic

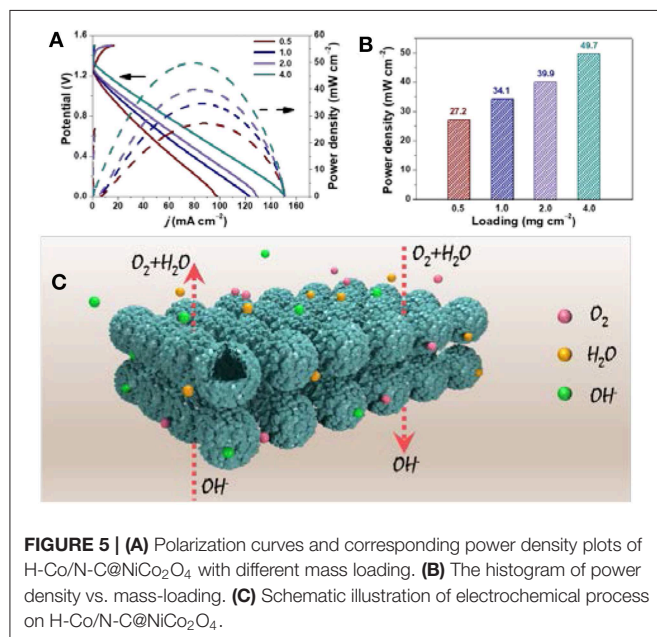


FIGURE 5 | (A) Polarization curves and corresponding power density plots of H-Co/N-C@NiCo₂O₄ with different mass loading. **(B)** The histogram of power density vs. mass-loading. **(C)** Schematic illustration of electrochemical process on H-Co/N-C@NiCo₂O₄.

effect of Co/N-C and NiCo₂O₄ guarantees promising bi-functional performance for both ORR and OER ($\Delta E = 0.82$ V). Second, the hierarchical structure provides large surface area, which enables fast charge transfer and more active sites accessible to electrolyte and O₂. Third, the hollow microsphere with sufficient internal void space and abundant mesopores serves as an efficient buffering reservoir and facilitates the fast diffusion of electrolyte. Last, this unique microsphere structure ensures good mechanical stability (more than 90 h) and minimizes particle aggregation, which is important to the practical application in ZAB (Figure 5C).

CONCLUSION

In summary, a hierarchical hollow structure H-Co/N-C@NiCo₂O₄ microsphere with cobalt/nitrogen-doped carbon as core and Ni-Co mixed metal oxides as shell has been successfully synthesized via a facile self-template approach. Benefiting from the advantages of this structure and composition, the H-Co/N-C@NiCo₂O₄ exhibits superior electrocatalytic activity and long-term stability for both ORR and OER. Furthermore, H-Co/N-C@NiCo₂O₄ is constructed as an air electrode for rechargeable ZAB, delivering a high power density and long cycling stability. The good linear relationship between the power density and various mass loading of H-Co/N-C@NiCo₂O₄ on the electrode demonstrates that the performance has been well-maintained even under high dense packing of catalysts,

which offers a new pathway for the practical applications in ZAB.

DATA AVAILABILITY STATEMENT

All datasets generated for this study are included in the manuscript/Supplementary Files.

AUTHOR CONTRIBUTIONS

MS conceived and supervised the project. YS and WX performed the experiment, characterized the materials, and wrote the manuscript supervised by JG and MS. SL performed the SEM characterization. All authors discussed the results and commented on the paper.

FUNDING

This work was supported by the National Natural Science Foundation of China (21601011 and 21521005) and the Fundamental Research Funds for the Central Universities (XK1802-6).

SUPPLEMENTARY MATERIAL

The Supplementary Material for this article can be found online at: <https://www.frontiersin.org/articles/10.3389/fmats.2019.00261/full#supplementary-material>

REFERENCES

- Aijaz, A., Masa, J., Rosler, C., Xia, W., Weide, P., Botz, A. J., et al. (2016). Co@Co₃O₄ encapsulated in carbon nanotube-grafted nitrogen-doped carbon polyhedra as an advanced bifunctional oxygen electrode. *Angew. Chem. Int. Ed.* 55, 4087–4091. doi: 10.1002/anie.201509382
- Amiinu, I. S., Liu, X., Pu, Z., Li, W., Li, Q., Zhang, J., et al. (2018). From 3D ZIF nanocrystals to Co-Nx/C nanorod array electrocatalysts for ORR, OER, and Zn-air batteries. *Adv. Funct. Mater.* 28, 1704638–1704646. doi: 10.1002/adfm.201704638
- Asset, T., Job, N., Busby, Y., Crisci, A., Martin, V., Stergiopoulos, V., et al. (2018). Porous hollow PtNi/C electrocatalysts: carbon support considerations to meet performance and stability requirements. *ACS Catal.* 8, 893–903. doi: 10.1021/acscatal.7b03539
- Audichon, T., Napporn, T. W., Canaff, C., Morais, C., Comminges, C., and Kokoh, K. B. (2016). IrO₂ coated on RuO₂ as efficient and stable electroactive nanocatalysts for electrochemical water splitting. *J. Phys. Chem. C* 120, 2562–2573. doi: 10.1021/acs.jpcc.5b11868
- Cao, C., Ma, D., Xu, Q., Wu, X., and Zhu, Q. (2018). Semisacrificial template growth of self-supporting MOF nanocomposite electrode for efficient electrocatalytic water oxidation. *Adv. Funct. Mater.* 29, 1807418–1807425. doi: 10.1002/adfm.201807418
- Chen, T., Zhang, Z., Cheng, B., Chen, R., Hu, Y., Ma, L., et al. (2017). Self-templated formation of interlaced carbon nanotubes threaded hollow Co₃S₄ nanoboxes for high-rate and heat-resistant lithium-sulfur batteries. *J. Am. Chem. Soc.* 139, 12710–12715. doi: 10.1021/jacs.7b06973
- Chen, X., Zhou, Z., Karahan, H. E., Shao, Q., Wei, L., and Chen, Y. (2018). Recent advances in materials and design of electrochemically rechargeable zinc-air batteries. *Small* 14, 1801929–1801957. doi: 10.1002/smll.201801929
- Cui, B., Lin, H., Liu, Y., Li, J.-B., Sun, P., Zhao, X., et al. (2009). Photophysical and photocatalytic properties of core-ring structured NiCo₂O₄ nanoplatelets. *J. Phys. Chem. C* 113, 14083–14087. doi: 10.1021/jp900028t
- Ferrero, G. A., Fuertes, A. B., Sevilla, M., and Titirici, M. M. (2016). Efficient metal-free N-doped mesoporous carbon catalysts for ORR by a template-free approach. *Carbon N. Y.* 106, 179–187. doi: 10.1016/j.carbon.2016.04.080
- Fu, Y., Yu, H., Jiang, C., Zhang, T., Zhan, R., Li, X., et al. (2018). NiCo alloy nanoparticles decorated on N-doped carbon nanofibers as highly active and durable oxygen electrocatalyst. *Adv. Funct. Mater.* 28, 1705094–1705103. doi: 10.1002/adfm.201705094
- Ganesan, P., Prabu, M., Sanetuntikul, J., and Shanmugam, S. (2015). Cobalt sulfide nanoparticles grown on nitrogen and sulfur codoped graphene oxide: an efficient electrocatalyst for oxygen reduction and evolution reactions. *ACS Catal.* 5, 3625–3637. doi: 10.1021/acscatal.5b00154
- Gu, C., Hu, S., Zheng, X., Gao, M. R., Zheng, Y. R., Shi, L., et al. (2018). Synthesis of sub-2 nm iron-doped NiSe₂ nanowires and their surface-confined oxidation for oxygen evolution catalysis. *Angew. Chem. Int. Ed.* 57, 4020–4024. doi: 10.1002/anie.201800883
- Guan, B. Y., Yu, L., and Lou, X. W. D. (2017). Formation of single-holed cobalt/N-doped carbon hollow particles with enhanced electrocatalytic activity toward oxygen reduction reaction in alkaline media. *Adv. Sci.* 4, 1700247–1700252. doi: 10.1002/advs.201700247
- Guan, C., Liu, X., Ren, W., Li, X., Cheng, C., and Wang, J. (2017). Rational design of metal-organic framework derived hollow NiCo₂O₄ arrays for flexible supercapacitor and electrocatalysis. *Adv. Energy Mater.* 7, 1602391–1602398. doi: 10.1002/aenm.201602391
- Guo, Y., Yuan, P., Zhang, J., Xia, H., Cheng, F., Zhou, M., et al. (2018). Co₂P-CoN double active centers confined in N-doped carbon nanotube: heterostructural engineering for trifunctional catalysis toward HER, ORR, OER, and Zn-air batteries driven water splitting. *Adv. Funct. Mater.* 28, 1805641–1805649. doi: 10.1002/adfm.201805641

- Guo, Z., Wang, F., Xia, Y., Li, J., Tamirat, A. G., Liu, Y., et al. (2018). *In situ* encapsulation of core-shell-structured $\text{Co}@\text{Co}_3\text{O}_4$ into nitrogen-doped carbon polyhedra as a bifunctional catalyst for rechargeable Zn-air batteries. *J. Mater. Chem. A* 6, 1443–1453. doi: 10.1039/C7TA09958D
- Hang, C., Zhang, J., Zhu, J., Li, W., Kou, Z., and Huang, Y. (2018). *In situ* exfoliating and generating active sites on graphene nanosheets strongly coupled with carbon fiber toward self-standing bifunctional cathode for rechargeable Zn-air batteries. *Adv. Energy Mater.* 8, 1703539–1703547. doi: 10.1002/aenm.201703539
- Jia, G., Zhang, W., Fan, G., Li, Z., Fu, D., Hao, W., et al. (2017). Three-dimensional hierarchical architectures derived from surface-mounted metal-organic framework membranes for enhanced electrocatalysis. *Angew. Chem. Int. Ed.* 56, 13781–13785. doi: 10.1002/anie.201708385
- Jiang, H., Liu, Y., Li, W., and Li, J. (2018). Co nanoparticles confined in 3D nitrogen-doped porous carbon foams as bifunctional electrocatalysts for long-life rechargeable Zn-air batteries. *Small* 14, 1703739–1703748. doi: 10.1002/smll.201703739
- Jiang, R., Li, L., Sheng, T., Hu, G., Chen, Y., and Wang, L. (2018). Edge-site engineering of atomically dispersed Fe-N₄ by selective C-N bond cleavage for enhanced oxygen reduction reaction activities. *J. Am. Chem. Soc.* 140, 11594–11598. doi: 10.1021/jacs.8b07294
- Kaneti, Y. V., Dutta, S., Hossain, M. S. A., Shiddiky, M. J. A., Tung, K. L., Shieh, F. K., et al. (2017). Strategies for improving the functionality of zeolitic imidazolate frameworks: tailoring nanoarchitectures for functional applications. *Adv. Mater. Weinheim* 29, 1700213–1700243. doi: 10.1002/adma.201700213
- Lee, J., Ha, J. U., Choe, S., Lee, C. S., and Shim, S. E. (2006). Synthesis of highly monodisperse polystyrene microspheres via dispersion polymerization using an amphiphilic initiator. *J. Colloid Interf. Sci.* 298, 663–671. doi: 10.1016/j.jcis.2006.01.001
- Lee, J. S., Tai Kim, S., Cao, R., Choi, N. S., Liu, M., Lee, K. T., et al. (2011). Metal-air batteries with high energy density: Li-air versus Zn-air. *Adv. Energy Mater.* 1, 34–50. doi: 10.1002/aenm.201000010
- Li, J., Lu, S. Q., Huang, H. L., Liu, D. H., Zhuang, Z. B., and Zhong, C. L. (2018). ZIF-67 as continuous self-sacrifice template derived $\text{NiCo}_2\text{O}_4/\text{Co,N-CNTs}$ nanocages as efficient bifunctional electrocatalysts for rechargeable Zn-air batteries. *ACS Sustainable Chem. Eng.* 6, 10021–10029. doi: 10.1021/acssuschemeng.8b01332
- Li, T., Lu, Y., Zhao, S., Gao, Z., and Song, Y. (2018). Co_3O_4 -doped Co/CoFe nanoparticles encapsulated in carbon shells as bifunctional electrocatalysts for rechargeable Zn-Air batteries. *J. Mater. Chem. A* 6, 3730–3737. doi: 10.1039/C7TA11171A
- Li, Y., and Dai, H. (2014). Recent advances in zinc-air batteries. *Chem. Soc. Rev.* 43, 5257–5275. doi: 10.1039/C4CS00015C
- Li, Y., Li, F. M., Meng, X. N., Li, S. N., Zeng, J. H., and Chen, Y. (2018). Ultrathin Co_3O_4 nanomeshes for the oxygen evolution reaction. *ACS Catal.* 8, 1913–1920. doi: 10.1021/acscatal.7b03949
- Li, Z., Shao, M., An, H., Wang, Z., Xu, S., Wei, M., et al. (2015). Fast electrosynthesis of Fe-containing layered double hydroxide arrays toward highly efficient electrocatalytic oxidation reactions. *Chem. Sci.* 6, 6624–6631. doi: 10.1039/C5SC02417J
- Li, Z., Shao, M., Zhou, L., Zhang, R., Zhang, C., Wei, M., et al. (2016). Directed growth of metal-organic frameworks and their derived carbon-based network for efficient electrocatalytic oxygen reduction. *Adv. Mater. Weinheim* 28, 2337–2344. doi: 10.1002/adma.201505086
- Liang, Q., Jin, H., Wang, Z., Xiong, Y., Yuan, S., Zeng, X., et al. (2019). Metal-organic frameworks derived reverse-encapsulation Co-NC@ Mo_2C complex for efficient overall water splitting. *Nano Energy* 57, 746–752. doi: 10.1016/j.nanoen.2018.12.060
- Liu, J., Zhu, D., Zheng, Y., Vasileff, A., and Qiao, S. Z. (2018). Self-supported earth-abundant nanoarrays as efficient and robust electrocatalysts for energy-related reactions. *ACS Catal.* 8, 6707–6732. doi: 10.1021/acscatal.8b01715
- Liu, Y., Dong, P., Li, M., Wu, H., Zhang, C., Han, L., et al. (2019). Cobalt nanoparticles encapsulated in nitrogen-doped carbon nanotube as bifunctional-catalyst for rechargeable Zn-air batteries. *Front. Mater.* 6, 85–101. doi: 10.3389/fmats.2019.00085
- Meng, F. L., Liu, K. H., Zhang, Y., Shi, M. M., Zhang, X. B., Yan, J. M., et al. (2018). Recent advances toward the rational design of efficient bifunctional air electrodes for rechargeable Zn-air batteries. *Small* 14, 1703843–1703862. doi: 10.1002/smll.201703843
- Ni, B., Ouyang, C., Xu, X., Zhuang, J., and Wang, X. (2017). Modifying commercial carbon with trace amounts of ZIF to prepare derivatives with superior ORR activities. *Adv. Mater. Weinheim* 29, 1701354–1701360. doi: 10.1002/adma.201701354
- Park, J., Park, M., Nam, G., Kim, M. G., and Cho, J. (2017). Unveiling the catalytic origin of nanocrystalline yttrium ruthenate pyrochlore as a bifunctional electrocatalyst for Zn-air batteries. *Nano Lett.* 17, 3974–3981. doi: 10.1021/acs.nanolett.7b01812
- Peng, S., Gong, F., Li, L., Yu, D., Ji, D., Zhang, T., et al. (2018). Necklace-like multishelled hollow spinel oxides with oxygen vacancies for efficient water electrolysis. *J. Am. Chem. Soc.* 140, 13644–13653. doi: 10.1021/jacs.8b05134
- Prabu, M., Ketpang, K., and Shanmugam, S. (2014). Hierarchical nanostructured NiCo_2O_4 as an efficient bifunctional non-precious metal catalyst for rechargeable zinc-air batteries. *Nanoscale* 6, 3173–3181. doi: 10.1039/c3nr05835b
- Qiu, H. J., Du, P., Hu, K., Gao, J., Li, H., Liu, P., et al. (2019). Metal and nonmetal codoped 3D nanoporous graphene for efficient bifunctional electrocatalysis and rechargeable Zn-air batteries. *Adv. Mater. Weinheim* 31, 1900843–1900849. doi: 10.1002/adma.201900843
- Shang, L., Yu, H., Huang, X., Bian, T., Shi, R., Zhao, Y., et al. (2016). Well-dispersed ZIF-derived Co,N-Co-doped carbon nanoframes through mesoporous-silica-protected calcination as efficient oxygen reduction electrocatalysts. *Adv. Mater. Weinheim* 28, 1668–1674. doi: 10.1002/adma.201505045
- Umeshbabu, E., Rajeshkhanna, G., Justin, P., and Rao, G. R. (2015). Synthesis of mesoporous NiCo_2O_4 -rGO by a solvothermal method for charge storage applications. *RSC Adv.* 5, 66657–66666. doi: 10.1039/C5RA11239G
- Wang, H. F., Tang, C., and Zhang, Q. (2018). A review of precious-metal-free bifunctional oxygen electrocatalysts: rational design and applications in Zn-air batteries. *Adv. Funct. Mater.* 28, 1803329–1803350. doi: 10.1002/adfm.201803329
- Wang, T., Kou, Z., Mu, S., Liu, J., He, D., Amiin, I. S., et al. (2018). 2D dual-metal zeolitic-imidazolate-framework-(ZIF)-derived bifunctional air electrodes with ultrahigh electrochemical properties for rechargeable zinc-air batteries. *Adv. Funct. Mater.* 28, 1705048–1705056. doi: 10.1002/adfm.201705048
- Wang, Z., Jin, H., Meng, T., Liao, K., Meng, W., Yang, J., et al. (2018). Fe, Cu-coordinated ZIF-derived carbon framework for efficient oxygen reduction reaction and zinc-air batteries. *Adv. Funct. Mater.* 28, 1802596–1802603. doi: 10.1002/adfm.201802596
- Wu, J., Zhang, J., Peng, Z., Yang, S., Wagner, F. T., and Yang, H. (2010). Truncated octahedral Pt_3Ni oxygen reduction reaction electrocatalysts. *J. Am. Chem. Soc.* 132, 4984–4985. doi: 10.1021/ja100571h
- Wu, R., Xiao, B., Gao, Q., Zheng, Y. R., Zheng, X. S., Zhu, J. F., et al. (2018). A janus nickel cobalt phosphide catalyst for high-efficiency neutral-pH water splitting. *Angew. Chem.* 57, 15445–15449. doi: 10.1002/anie.201808929
- Xie, W. F., Li, Z. H., Jiang, S., Li, J. B., Shao, M. F., and Wei, M. (2019). Mass-loading independent electrocatalyst with high performance for oxygen reduction reaction and Zn-air battery based on Co-N-codoped carbon nanotube assembled microspheres. *Chem. Eng. J.* 373, 734–743. doi: 10.1016/j.cej.2019.04.066
- Yang, Q. H., Li, Z. H., Zhang, R. K., Zhou, L., Shao, M. F., and Wei, M. (2017). Carbon modified transition metal oxides/hydroxides nanoarrays toward high-performance flexible all-solid-state supercapacitors. *Nano Energy* 41, 408–416. doi: 10.1016/j.nanoen.2017.09.049
- Zhan, G., and Zeng, H. C. (2017). ZIF-67-derived nanoreactors for controlling product selectivity in CO_2 hydrogenation. *ACS Catal.* 7, 7509–7519. doi: 10.1021/acscatal.7b01827
- Zhang, C., Fu, L., Liu, N., Liu, M., Wang, Y., and Liu, Z. (2011). Synthesis of nitrogen-doped graphene using embedded carbon and nitrogen sources. *Adv. Mater. Weinheim* 23, 1020–1024. doi: 10.1002/adma.201004110
- Zhang, G., and Lou, X. W. (2013). General solution growth of mesoporous NiCo_2O_4 nanosheets on various conductive substrates as high-performance electrodes for supercapacitors. *Adv. Mater. Weinheim* 25, 976–979. doi: 10.1002/adma.201204128

- Zhang, J., Wang, T., Pohl, D., Rellinghaus, B., Dong, R., Liu, S., et al. (2016). Interface engineering of MoS₂/Ni₃S₂ heterostructures for highly enhanced electrochemical overall-water-splitting activity. *Angew. Chem. Int. Ed.* 55, 6702–6707. doi: 10.1002/anie.201602237
- Zhao, D., Shui, J. L., Chen, C., Chen, X., Repogle, B. M., Wang, D., et al. (2012). Iron imidazolate framework as precursor for electrocatalysts in polymer electrolyte membrane fuel cells. *Chem. Sci.* 3, 3200–3205. doi: 10.1039/c2sc20657a
- Zhou, L., Shao, M., Zhang, C., Zhao, J., He, S., Rao, D., et al. (2017b). Hierarchical CoNi-sulfide nanosheet arrays derived from layered double hydroxides toward efficient hydrazine electrooxidation. *Adv. Mater. Weinheim.* 29, 1604080–1604087. doi: 10.1002/adma.201604080
- Zhou, L., Shao, M. F., Li, J. B., Jiang, S., Wei, M., and Duan, X. (2017a). Two-dimensional ultrathin arrays of CoP: electronic modulation toward high performance overall water splitting. *Nano Energy* 41, 583–590. doi: 10.1016/j.nanoen.2017.10.009
- Zhou, W., Wu, X., Cao, X., Huang, X., Tan, C., Tian, J., et al. (2013). Ni₃S₂ nanorods/Ni foam composite electrode with low overpotential for electrocatalytic oxygen evolution. *Energy Environ. Sci.* 6, 2921–2924. doi: 10.1039/c3ee41572d

Conflict of Interest: The authors declare that the research was conducted in the absence of any commercial or financial relationships that could be construed as a potential conflict of interest.

Copyright © 2019 Song, Xie, Li, Guo and Shao. This is an open-access article distributed under the terms of the Creative Commons Attribution License (CC BY). The use, distribution or reproduction in other forums is permitted, provided the original author(s) and the copyright owner(s) are credited and that the original publication in this journal is cited, in accordance with accepted academic practice. No use, distribution or reproduction is permitted which does not comply with these terms.